International Asteroid Warning Network Timing Campaign: 2019 XS

Davide Farnocchia[1], Vishnu Reddy[2], James M. Bauer[3], Elizabeth M. Warner[3], Marco Micheli[4], Matthew J. Payne[5], Tony Farnham[3], Michael S. Kelley[6], David D. Balam[7], Anatoly P. Barkov[8], Daniel Berteşteanu[9], Mirel Birlan[10,11], Bryce T. Bolin[12,13], Melissa J. Brucker[2], Luca Buzzi[14], Kenneth C. Chambers[15], Lukas Demetz[16], Anlaug A. Djupvik[17,18], Leonid Elenin[19], Paolo Fini[20], Randy Flynn[21], Gianni Galli[22], Xing Gao[23], Marcin Gędek[24], Mikael Granvik[25,26], Werner Hasubick[27], Alexander L. Ivanov[8], Viktor A. Ivanov[8], Natalya V. Ivanova[28], Cristóvão Jaques[29], Anni Kasikov[17,18,30], Myung-Jin Kim[31], David Lane[32], Hee-Jae Lee[31], Bin Li[33,34], Fan Li[33,34], Tim Lister[35], Vadim E. Lysenko[8], Eugene A. Magnier[15], Nawaz Mahomed[36], Jennie McCormick[37], Darrel Moon[38], Alessandro Nastasi[39], Dan A. Nedelcu[10,11], Guenther Neue[40], Elisabeta Petrescu[4,41], Marcel Popescu[42], Enrico Prosperi[43], Rafał Reszelewski[24], Dong-Goo Roh[31], Filipp D. Romanov[44,45], Toni Santana-Ros[46,47], Anastasia Schmalz[48], Sergei Schmalz[48], James V. Scotti[2], Robert Seaman[2], Nick Sioulas[49], Adrian B. Sonka[10], David J. Tholen[15], Madalina M. Trelia[50,51], Richard Wainscoat[15], Xin Wang[33], Guy Wells[52], Robert Weryk[53], Nikolai A. Yakovenko[8], Quanzhi Ye[3], Hong-Suh Yim[31], Chengxing Zhai[1], Chen Zhang[33,34], Haibin Zhao[33], Tinglei Zhu[33], and Michał Żołnowski[24]

[1] Jet Propulsion Laboratory, California Institute of Technology, 4800 Oak Grove Drive, Pasadena, CA 91109, USA; Davide.Farnocchia@jpl.nasa.gov
[2] Lunar and Planetary Laboratory, University of Arizona, 1629 E. University Boulevard, Tucson, AZ 85721, USA
[3] University of Maryland, 4296 Stadium Drive, Astronomy Dept., Room 1113, College Park, MD 20742, USA
[4] ESA NEO Coordination Centre, Largo Galileo Galilei, 1, I-00044 Frascati (RM), Italy
[5] Harvard-Smithsonian Center for Astrophysics, 60 Garden Street, MS 51, Cambridge, MA 02138, USA
[6] Planetary Defense Coordination Office, Planetary Science Division, NASA Headquarters, 300 East Street SW, Washington, DC 20546, USA
[7] Dominion Astrophysical Observatory, National Research Council of Canada, 5071 West Saanich Road, Victoria, BC V9E 2E7, Canada
[8] Kuban State University, Stavropolskaya Street, 149, Krasnodar 350040, Russia
[9] Astroclubul Bucureşti, 21 Lascăr Catargiu blvd, Sector 1, 010662 Bucharest, Romania
[10] Astronomical Institute of the Romanian Academy, str Cutitul de Argint—5, 040557, Bucharest, Romania
[11] Institut de mécanique céleste et de calcul des Ephémérides, CNRS8024, Observatoire de Paris, 77 av Denfert Rocherau, F-75014 Paris, France
[12] Division of Physics, Mathematics, and Astronomy, California Institute of Technology, 1200 E. California Boulevard, Pasadena, CA 91125, USA
[13] Infrared Processing and Analysis Center, California Institute of Technology, 1200 E. California Boulevard, Pasadena, CA 91125, USA
[14] Schiaparelli Astronomical Observatory, Campo dei Fiori, Varese, VA I-21100, Italy
[15] Institute for Astronomy, University of Hawaii, 2680 Woodlawn Drive, Honolulu, HI 96822, USA
[16] Skygems Observatory Network, Cisles 51, Santa Cristina Valgardena, BZ I-39047, Italy
[17] Nordic Optical Telescope, Rambla José Ana Fernández Pérez 7, E-38711 Breña Baja, Spain
[18] Department of Physics and Astronomy, Aarhus University, Ny Munkegade 120, DK-8000 Aarhus C, Denmark
[19] Keldysh Institute of Applied Mathematics of Russian Academy of Sciences, Miusskaya sq., 4, Moscow, 125047, Russia
[20] Gruppo Astrofili Montelupo, Via San Vito 60, I-50056 Montelupo Fiorentino (FI), Italy
[21] Squirrel Valley Observatory, 3870 River Road, Columbus, NC 28722, USA
[22] GiaGa Observatory, Via Mozart 4, I-20005 Pogliano Milanese (MI), Italy
[23] Xinjiang Astronomical Observatory, 150 Science One St, Ürümqi, Xinjiang Uyghur Autonomous Region 830011, People's Republic of China
[24] 6ROADS Ltd., Godebskiego 55a Street, 31-999 Cracow, Poland
[25] Department of Physics, P.O. Box 64, FI-00014 University of Helsinki, Finland
[26] Asteroid Engineering Lab, Luleå University of Technology, Box 848, SE-98128 Kiruna, Sweden
[27] Public Observatory Buchloe, Alois-Reiner-Str. 15b, D-86807 Buchloe, Germany
[28] National Astronomical Agency, Zheleznodorozhnaya street 1, Afipsky village, Krasnodar Territory, Russia
[29] Southern Observatory for Near Earth Asteroids Research, Oliveira, Brazil
[30] Tartu Observatory, University of Tartu, Observatooriumi 1, Tõravere, 61602, Estonia
[31] Korea Astronomy and Space Science Institute, 776, Daedeokdae-ro, Yuseong-gu, Daejeon 34055, Republic of Korea
[32] Burke-Gaffney Observatory, Saint Mary's University, 923 Robie Street, Halifax, NS B3H 3C3, Canada
[33] Purple Mountain Observatory, Chinese Academy of Sciences, Nanjing, 210023, People's Republic of China
[34] University of Science and Technology of China, Hefei, 230026, People's Republic of China
[35] Las Cumbres Observatory, 6740 Cortona Drive, Suite 102, Goleta, CA 93117, USA
[36] Department of Mechanical and Mechatronic Engineering, Stellenbosch University, Cnr Banghoek Road and Joubert Street, Stellenbosch 7600, South Africa
[37] Farm Cove Observatory, 2/24 Rapallo Place, Farm Cove, Auckland 2010, New Zealand
[38] Killer Rocks Observatory, HC 65 Box 2, Pie Town, NM 87827, USA
[39] GAL Hassin—Centro Internazionale per le Scienze Astronomiche, Via della Fontana Mitri, I-90010 Isnello (PA), Italy
[40] Wickede Observatory, Stemmering 5, D-44319 Dortmund, Germany
[41] ESA ESOC Space Safety Service Centre, Robert-Bosch-Straße 5, D-64293, Darmstadt, Germany
[42] Astronomical Institute of the Romanian Academy, 5 Cuţitul de Argint, 040557 Bucharest, Romania
[43] Osservatorio di Castelmartini, via Bartolini 1317, Larciano, Pistoia, I-51036, Italia
[44] Amateur astronomer, Russia
[45] Remote observer of Burke-Gaffney Observatory and Abbey Ridge Observatory, Canada
[46] Institut de Ciències del Cosmos, Universitat de Barcelona, Carrer de Martí i Franquès, 1, E-08028 Barcelona, Spain
[47] Departamento de Física, Ingeniería de Sistemas y Teoría de la Señal, Universidad de Alicante, Carr. de San Vicente del Raspeig, s/n, 03690 San Vicente del Raspeig, Alicante, Spain
[48] Keldysh Institute of Applied Mathematics, Russian Academy of Sciences, Miusskaya sq. 4, Moscow, 125047, Russia
[49] NOAK Observatory, Delfon 2 Stavraki, Ioannina, 45500, Greece
[50] Romanian Space Agency, str Mendeleev 25, 010362, Bucharest, Romania
[51] University of Bucharest, Faculty of Physics, str Atomistilor 405, 077125 Magurele, Romania

[52] Northolt Branch Observatories, Dabbs Hill Lane, Northolt, London, UK
[53] Physics and Astronomy, The University of Western Ontario, 1151 Richmond Street, London, ON N6A 3K7, Canada

Abstract

As part of the International Asteroid Warning Network's observational exercises, we conducted a campaign to observe near-Earth asteroid 2019 XS around its close approach to Earth on 2021 November 9. The goal of the campaign was to characterize errors in the observation times reported to the Minor Planet Center, which become an increasingly important consideration as astrometric accuracy improves and more fast-moving asteroids are observed. As part of the exercise, a total of 957 astrometric observations of 2019 XS during the encounter were reported and subsequently were analyzed to obtain the corresponding residuals. While the timing errors are typically smaller than 1 s, the reported times appear to be negatively biased, i.e., they are generally earlier than they should be. We also compared the observer-provided position uncertainty with the cross-track residuals, which are independent of timing errors. A large fraction of the estimated uncertainties appear to be optimistic, especially when $<0\rlap{.}''2$. We compiled individual reports for each observer to help identify and remove the root cause of any possible timing error and improve the uncertainty quantification process. We suggest possible sources of timing errors and describe a simple procedure to derive reliable, conservative position uncertainties.

Unified Astronomy Thesaurus concepts: Asteroids (72); Near-Earth objects (1092); Optical telescopes (1174); Astrometry (80)

1. Introduction

The International Asteroid Warning Network (IAWN) was established with the goal of assessing, strengthening, and coordinating the international response to a possible near-Earth object (NEO) impact threat.[54] As part of its mission, IAWN has organized observation campaign exercises to observe NEOs with orbits that come within 0.05 au of that of Earth. The first observation campaign took place in 2017 and targeted asteroid 2012 TC4.[55] The goals of this campaign were the recovery, tracking, and physical characterization prior to the 2017 October close approach to Earth (Reddy et al. 2019). The second campaign targeted binary asteroid (66391) 1999 KW4 during the 2019 apparition.[56] Given the very well constrained orbit of (66391), the campaign mostly focused on physical characterization (Reddy et al. 2022a). The third campaign targeted (99942) Apophis during the 2020–2021 apparition.[57] Apophis was treated as an unknown asteroid, and thus the campaign simulated the discovery, follow-up, characterization, and impact hazard assessment for the 2029 encounter (Reddy et al. 2022b).

Understanding and characterizing astrometric observation errors is key to enabling accurate trajectory estimation for asteroids. Over the years significant effort has been devoted to statistically analyzing the quality of the data and devising suitable statistical treatments to be used in the orbit determination process (Carpino et al. 2003; Chesley et al. 2010; Farnocchia et al. 2015; Vereš et al. 2017; Eggl et al. 2020). Because of the lack of observer-provided uncertainty information for optical astrometry, weighting schemes have relied on an observing site's historical performance to determine the data weights. The new ADES format of the International Astronomical Union (IAU; Chesley et al. 2017)[58] provides observers the ability to report observational uncertainties, along with other metadata, and therefore represents the beginning of a new era in terms of data treatment. This new format is the next-generation reporting standard accepted by the Minor Planet Center (MPC), the IAU's designated clearinghouse of astrometric observations of small bodies.

Advances in instrumentation capabilities and in the accuracy of star catalogs (e.g., Gaia Collaboration et al. 2018, 2021) have led to increasing accuracy of astrometric observations, and timing errors have become a consideration, especially for fast-moving objects. In fact, a timing error maps into a positional error proportional to the plane-of-sky rate of motion. The effect of timing errors was particularly evident in the observations of 2021 TC4 collected during the 2017 October encounter to Earth, when 2012 TC4 reached a plane-of-sky rate of motion of almost $20''\,s^{-1}$ and astrometric errors in some cases exceeded $10''$ (Reddy et al. 2019). Given the increasing number of observations of targets moving at high rates of motion (e.g., see rate of motion of recent NEO discoveries in Vereš et al. 2018), timing errors become a more important source of error. Therefore, we decided to conduct a campaign with the goal of assessing the accuracy of the observation times reported to the Minor Planet Center.

2. Target Selection

In 2021 September, we searched the asteroid catalog to identify viable targets for a timing campaign. Asteroid 2019 XS stood out as the best candidate because of the following properties:

1. A close approach to Earth on 2021 November 9 at 1.5 lunar distances from the geocenter.
2. A peak plane-of-sky rate of motion of $3\rlap{.}''8\,s^{-1}$.
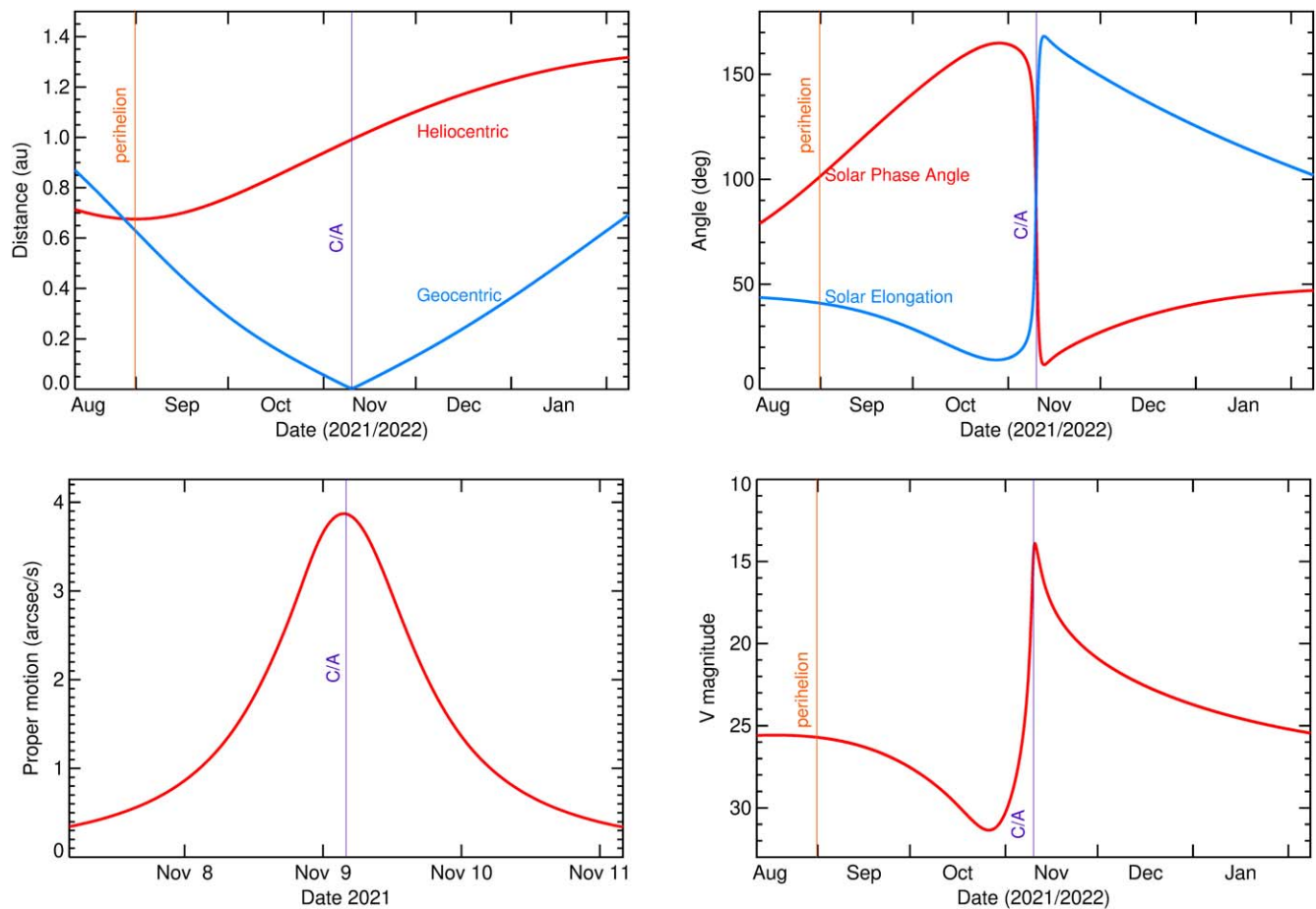

Figure 1. 2019 XS geocentric and heliocentric distance (top left), solar elongation and phase angle (top right), plane-of-sky rate of motion (bottom left), and *V*-band magnitude (bottom right) as a function of time. The vertical lines correspond to the time of perihelion and time of closest approach to Earth.

3. A peak brightness of *V* magnitude < 14, making 2019 XS detectable even with modest instrumentation.
4. Small orbital uncertainties (MPC uncertainty parameter U[59] of 0), which ensure that observation residuals are reflective of observation errors.

Figures 1 and 2 show the observing conditions of 2019 XS during the 2021 apparition. 2019 XS approached Earth at a small solar elongation, was not observable until the day prior to the close approach, and was in the nighttime sky after the close approach. During the encounter, 2019 XS was in the southern sky and was therefore more challenging to observe from the Northern Hemisphere, where most telescopes tracking asteroids are located.

Before the start of the observation campaign, precovery observations from the Sloan Digital Sky Survey were reported to the MPC (MPEC 2021-T202)[60] and further reduced the orbital uncertainties. Moreover, 2019 XS was observed by radar on 2021 November 11 and 13,[61,62] which also refined the orbit, thus enabling a more reliable assessment of astrometric residuals.

3. Observations

During the 2021 apparition, 2019 XS was first observed by SpringBok observatory (MPEC 2021-V183)[63] on 2021 November 8 and extensively tracked for the following days. Campaign participants were asked to disclose their intent to participate to IAWN. The exercise was announced through a publicly released MPEC,[64] and the observations were to be received at the MPC by 2021-11-12.0 UT. Participants were briefed on the procedures and preliminary outcomes of the campaign in a series of telecons and through postings on the campaign's website.[65] The complete observation data set is available from the MPC.[66] In this paper, we focus on the 957 observations that we collected as part of this campaign from 2021-11-08.0 to 2021-11-12.0 UTC, when the plane-of-sky rate of motion was large enough (see bottom left panel Figure 1) to probe the accuracy of the reported observation times. Table 1 lists the 71 observatories that contributed observations to support this observation campaign, and, except for the space-based C53, Figure 3 shows their geographical locations, which provided extensive longitudinal coverage.

[59] https://www.minorplanetcenter.net/iau/info/UValue.html
[60] https://www.minorplanetcenter.net/mpec/K21/K21TK2.html
[61] https://ssd.jpl.nasa.gov/sb/radar.html
[62] https://echo.jpl.nasa.gov/asteroids/Orpheus/Orpheus.2021.goldstone.planning.html

[63] https://www.minorplanetcenter.net/mpec/K21/K21VI3.html
[64] https://www.minorplanetcenter.net/mpec/K21/K21T79.html
[65] https://iawn.net/obscamp/2019XS/
[66] https://minorplanetcenter.net/db_search/show_object?utf8=%E2%9C%93&object_id=2019+XS
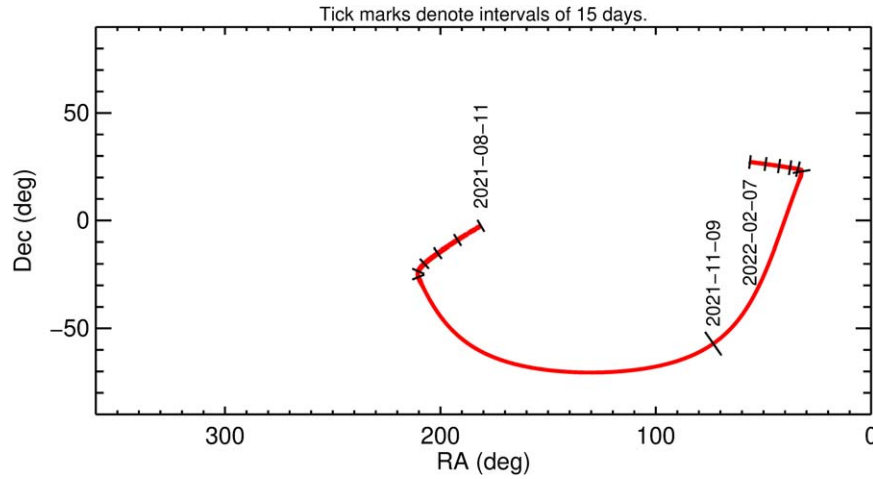
Figure 2. 2019 XS R.A. and decl. as a function of time.

We reported the majority (543) of the campaign observations to the MPC in the ADES format (Chesley et al. 2017), including uncertainty information to inform the orbit determination process. The observations in ADES format are available from the MPC.[67,68,69,70,71,72,73]

4. Reference Orbit Solution

The first step in the analysis was to estimate an accurate orbit for 2019 XS against which to compute the residuals. We included all the data prior to 2021 and after 2021-11-13.5 UTC, which we weighted based on the Vereš et al. (2017) weighting scheme, except for the Pan-STARRS and Sloan precoveries, which we weighted at $0''5$ and $1''5$, respectively. We also applied the Eggl et al. (2020) debiasing scheme to correct for star catalog systematic errors. The Pan-STARRS 2019 detection has arcsecond-level residuals, which is significantly worse than its typical astrometric accuracy (Vereš et al. 2017), and so was rejected as an outlier.

The vast majority of the data around the encounter were not used in the fit to keep timing errors from affecting the orbit estimate and to avoid biasing the orbit solution toward the observations collected during the campaign. We only retained a handful of observations with the purpose of validating and calibrating the solution:

1. a single position from L80 on 2021 November 8;
2. a single position from W98, Q63, Q58, and Z84 on 2021 November 9;
3. a single position from V15 and Q12 on 2021 November 10;
4. a single position from N50 and C65 and two positions (one per tracklet) from T12 on 2021 November 11; and
5. a single position from Z23 and T12 on 2021 November 12.

These observations were selected based on the track record of the observers, in terms of astrometric position accuracy, astrometric uncertainty accuracy, and timing errors. In particular, these observers regularly check their estimated observation times against GPS satellites.[74]

For all observations we assumed a time uncertainty of 1 s. The only exception were the two T12 detections on 2021 November 11, for which timing was calibrated using GPS satellites, and we therefore assumed a 0.1 s uncertainty. Time uncertainties can be included in an observation's weight by decomposing the total error Δ in R.A. α and decl. δ:

$$\begin{pmatrix} \Delta\alpha \\ \Delta\delta \end{pmatrix} = \begin{pmatrix} \Delta\alpha_P \\ \Delta\delta_P \end{pmatrix} - \begin{pmatrix} \dot\alpha \\ \dot\delta \end{pmatrix}\Delta T, \qquad (1)$$

where the subscript P refers to the position measurement error, $\dot\alpha$ and $\dot\delta$ are the plane-of-sky rates of motion, and ΔT is the timing error. $\Delta\alpha$, $\Delta\alpha_P$, and $\dot\alpha$ all include the spherical metric factor $\cos\delta$. It is worth noting that $\dot\alpha$ and $\dot\delta$ are a function of the current orbit solution and therefore can (slightly) change during the iterative differential correction process. By assuming that the position measurement error and the timing error are independent, the total covariance can be computed as $C = C_P + C_T$, where C_P is the (not necessarily diagonal) position measurement covariance,

$$C_T = \sigma_T^2 \begin{pmatrix} \dot\alpha^2 & \dot\alpha\dot\delta \\ \dot\alpha\dot\delta & \dot\delta^2 \end{pmatrix},$$

and σ_T is the time uncertainty. The inverse of the augmented covariance C is then used to weight the observation in the least-squares process.

The long optical observation arc from 2000 to 2021 and the radar observations collected right after the 2021 close approach result in an extremely well constrained orbit, e.g., the 1σ formal uncertainty in semimajor axis is only 600 m, which corresponds to 0.2 s in orbital period. In order to fit the data, we also had to include and estimate the Yarkovsky effect (Vokrouhlický et al. 2015), which we modeled as a transverse acceleration A_2/r^2, where r is the heliocentric distance in au (Farnocchia et al. 2013). Table 2 shows the best-fit orbit

[67] https://minorplanetcenter.net/mpec/K21/K21VK0.xml
[68] https://minorplanetcenter.net/mpec/K21/K21VO7.xml
[69] https://minorplanetcenter.net/mpec/K21/K21VR4.xml
[70] https://minorplanetcenter.net/mpec/K21/K21VU2.xml
[71] https://minorplanetcenter.net/mpec/K21/K21VV5.xml
[72] https://minorplanetcenter.net/mpec/K21/K21Y11.xml
[73] https://minorplanetcenter.net/mpec/K21/K21Y53.xml

[74] https://www.projectpluto.com/gps_expl.htm

Table 1
List of Participating Observatories and Number of Observations Collected as Part of the Campaign between 2021-11-08.0 UTC and 2021-11-12.0 UTC

Code	Name	N Obs.	Code	Name	N Obs.
073	Bucharest	90	M33	OWL-Net, Mitzpe Ramon	6
160	Castelmartini	9	N50	Himalayan Chandra Telescope, IAO, Hanle	8
186	Kitab	14	N82	Multa Observatory	18
203	GiaGa Observatory	4	N88	Xingming Observatory #3, Nanshan	36
215	Buchloe	6	O48	Purple Mountain Observatory, Yaoan (0.8 m)	48
291	LPL/Spacewatch II	18	O49	Purple Mountain Observatory, Yaoan Station	17
595	Farra d'Isonzo	10	Q12	Nagano Observatory	4
654	Table Mountain Observatory, Wrightwood-PHMC	10	Q58	Siding Spring-LCO Clamshell #1	5
691	Steward Observatory, Kitt Peak-Spacewatch	12	Q63	Siding Spring-LCO A	11
703[†]	Catalina Sky Survey	8	T03	Haleakala-LCO Clamshell #3	7
851	Burke-Gaffney Observatory, Halifax	20	T04	Haleakala-LCO OGG B #2	7
A50	Andrushivka Astronomical Observatory	19	T05[†]	ATLAS-HKO, Haleakala	5
C40	Kuban State University Astrophysical Observatory	12	T08[†]	ATLAS-MLO, Mauna Loa	21
C53	NEOSSat	36	T12	Maunakea-UH/Tholen NEO Follow-Up (2.24 m)	10
C65	Observatori Astronomic del Montsec	12	V06	Catalina Sky Survey-Kuiper	7
D05	ISON-Terskol Observatory	9	V15	OWL-Net, Mt. Lemmon	6
D29[†]	Purple Mountain Observatory, XuYi Station	54	V17	Leo Observatory, Tucson	7
E85	Farm Cove	11	V19	Whiskey Creek Observatory	3
F51[†]	Pan-STARRS 1, Haleakala	12	V20	Killer Rocks Observatory, Pie Town	8
F52[†]	Pan-STARRS 2, Haleakala	8	V37	McDonald Observatory-LCO ELP	7
G33	Wickede	13	V38	McDonald Observatory-LCO ELP Aqawan A #1	10
G34	Oberfrauendorf	28	V39	McDonald Observatory-LCO ELP B	5
G96[†]	Mt. Lemmon Survey	12	W34	Squirrel Valley Observatory, Columbus	4
I22	Abbey Ridge Observatory, Stillwater Lake	40	W85	Cerro Tololo-LCO A	7
I41	Palomar Mountain—ZTF	5	W86	Cerro Tololo-LCO B	23
I52	Steward Observatory, Mt. Lemmon Station	7	W98	Polonia Observatory, San Pedro de Atacama	7
K91	Sutherland-LCO A	5	Y00	SONEAR Observatory, Oliveira	7
K92	Sutherland-LCO B	7	Z23	Nordic Optical Telescope, La Palma	13
K93	Sutherland-LCO C	7	Z24	Tenerife Observatory-LCO B, Tenerife	7
L02	NOAK Observatory, Stavraki	4	Z28	Northern Skygems Observatory, Nerpio	3
L09	Sutherland-LCO Aqawan A #1	8	Z31	Tenerife Observatory-LCO A, Tenerife	7
L34	Galhassin Robotic Telescope, Isnello	3	Z33	6ROADS Observatory 2, Nerpio	7
L54	Berthelot Observatory, Hunedoara	63	Z43	Landehen	4
L73	Beato Ermanno Observatory, Impruneta	4	Z80	Northolt Branch Observatory	6
L80	SpringBok Observatory, Tivoli	8	Z84	Calar Alto-Schmidt	12
L81	Skygems Namibia Remote Observatory	6			

Note. A dagger symbol indicates surveys.

solution, which we used as reference to compute the astrometric residuals.

5. Analysis of the Residuals

The astrometric residuals in R.A. r_α (scaled by $\cos\delta$) and decl. r_δ can conveniently be mapped into along-track and cross-track residuals r_{AT} and r_{CT}. The unit vectors

$$v_{AT} = \frac{1}{\sqrt{\dot{\alpha}^2 + \dot{\delta}^2}} \begin{pmatrix} \dot{\alpha} \\ \dot{\delta} \end{pmatrix}, \quad v_{CT} = \frac{1}{\sqrt{\dot{\alpha}^2 + \dot{\delta}^2}} \begin{pmatrix} -\dot{\delta} \\ \dot{\alpha} \end{pmatrix}$$

are aligned with and normal to, respectively, the plane-of-sky motion of the asteroid. The along-track and cross-track residuals can be computed as

$$r_{AT} = \begin{pmatrix} r_\alpha \\ r_\delta \end{pmatrix} \cdot v_{AT}, \quad r_{CT} = \begin{pmatrix} r_\alpha \\ r_\delta \end{pmatrix} \cdot v_{CT}.$$

In a similar way, the positional uncertainties in the cross-track and along-track components are

$$\sigma_{AT} = \sqrt{v_{AT}^t C_P v_{AT}}, \quad \sigma_{CT} = \sqrt{v_{CT}^t C_P v_{CT}}.$$

The advantage of this decomposition is that the cross-track component is independent of timing errors and is therefore purely caused by astrometric position error. On the other hand, timing errors fully map onto the along-track component. Therefore, by projecting Equation (1) along v_{AT}, the timing error can be estimated as $r_T = -r_{AT} / \sqrt{\dot{\alpha}^2 + \dot{\delta}^2}$, with an uncertainty $\sigma_T = \sigma_{AT} / \sqrt{\dot{\alpha}^2 + \dot{\delta}^2}$.

Figure 4 shows the cross-track and along-track residuals for the 921 ground-based observations collected during the campaign as a function of the plane-of-sky rate of motion. The residuals of the 36 observations from NEOSSat could not be mapped into the along-track and cross-track components because the velocity of the observer is not currently reported to the MPC for space-based observations, and therefore they are ignored in the analysis presented in this section. The vast majority of cross-track residuals are $<1''$, with errors that are not correlated with the rate of motion. The along-track residuals can be significantly larger in size, especially as the rate of motion increases. However, it is worth noting that some observers achieve subarcsecond along-track errors even at large rates of motion, which suggests their accurate recording of the observation time.
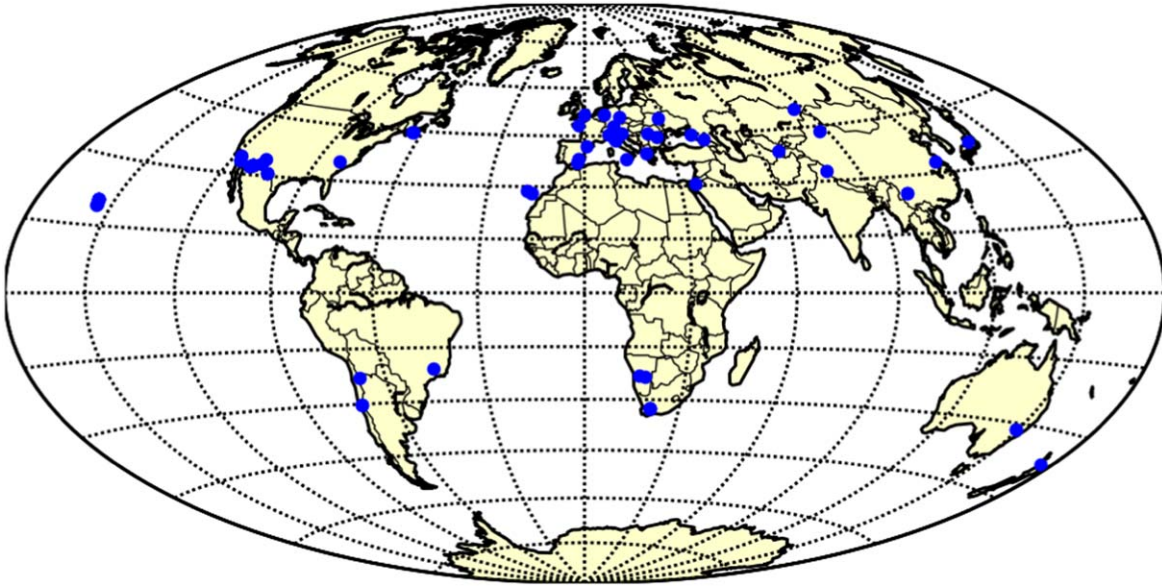
Figure 3. Locations of the 70 ground-based observation sites that participated in the campaign.

Table 2
JPL Orbit Solution 30

Parameter	Value
Eccentricity	$0.3289780465 \pm 1.71 \times 10^{-8}$
Perihelion distance (au)	$0.6744210503 \pm 1.74 \times 10^{-8}$ au
Time of perihelion (TDB, days)	2021-08-30.83212273 TDB $\pm 1.05 \times 10^{-6}$ days
Longitude of node	$49.57013106 \pm 1.44 \times 10^{-6}$ deg
Argument of perihelion	$250.13485868 \pm 2.17 \times 10^{-6}$ deg
Inclination	$4.31382506 \pm 4.07 \times 10^{-6}$ deg
Yarkovsky parameter A_2	$-16.70 \times 10^{-14} \pm 1.64 \times 10^{-14}$ au day^{-2}

Note. The osculating epoch is 2021 November 9 TDB, and the orbital elements refer to the IAU76 ecliptic frame (Seidelmann 1977). Error bars correspond to formal 1σ uncertainties. The solution is based on 129 optical observations from 2000 April 4 to 2021 December 9, four radar delay observations, and one radar Doppler observation.

For each observer, we grouped the observations in tracklets by using a 0.1-day gap between consecutive observations as the cutoff for splitting. For each tracklet, we analyzed the residuals in the along-track and cross-track directions. Figure 5 shows an example of a tracklet with well-behaved residuals. Cross-track residuals (left panel) do not show any particular bias and are well consistent with the estimated uncertainties. In fact, the weighted rms of the cross-track residuals

$$\mathrm{rms_{CT}} = \sqrt{\sum_{i=1}^{N}\left(\frac{(r_{CT})_i}{(\sigma_{CT})_i}\right)^2 \Big/ N}$$

is 0.7. The timing errors (right panel) are also unbiased and can be fully explained by positional errors within the reported uncertainties. Therefore, there is no indication of a significant timing error for this tracklet.

On the other hand, Figure 6 shows an example of a tracklet that displays some issues. The estimated uncertainties do not capture the extent of the residuals. The weighted rms of 2 indicates that uncertainties are underestimated by a factor of about 2. The timing residuals display a clear bias, which can be

estimated as $b_T \pm \sigma_{b_T}$, where

$$b_T = \sum_i \frac{(r_T)_i}{(\sigma_T)_i^2} \Big/ \sum_i \frac{1}{(\sigma_T)_i^2}, \quad \sigma_{b_T} = \sqrt{\left(1 \Big/ \sum_i \frac{1}{(\sigma_T)_i^2}\right)^{-1}}.$$

For this specific tracklet we obtain $b_T = -0.66 \pm 0.05$ s, which cannot be explained by the uncertainties of the orbital solution (see right panel of Figure 6).

Individual reports have been compiled for each observer to assess the quality of the reported observations and identify possible problems with timing and position uncertainty estimates. Here we focus on providing a comprehensive statistical analysis of the campaign data. For each tracklet, the left plane of Figure 7 shows the weighted rms of the cross-track residuals as a function of the astrometric position uncertainty. A weighted rms smaller than 1 indicates that position uncertainties are too conservative, while a weighted rms greater than 1 indicates that position uncertainties underestimate the true errors. Table 3 shows the fraction of tracklets with weighted rms greater than 1 for different uncertainty intervals. For uncertainties larger than $0.''5$ most observations have conservative uncertainties, which is not surprising. In fact, this bin is dominated by observations where no uncertainty was reported, and therefore the Vereš et al. (2017) data weights were used, which are designed to be conservative. As the reported uncertainties decrease, they generally become optimistic and underestimate the actual errors, possibly because some sources of error are being neglected in the uncertainty assessment.

The right panel of Figure 7 shows the estimated time bias for the tracklets of observations collected during the campaign. Besides the tracklet-specific timing biases properly communicated to the individual observers, there seems to be an overall predominance of negative time errors, i.e., the reported time is earlier than it should be. Though in some cases this error is as large as a couple seconds, for the most part the timing error is within 1 s. Surveys have timing errors consistently within $\sim$1 s. However, it is important to point out that trailing could significantly contribute to the along-track error (Vereš et al. 2012). Thanks to the brightness of 2019 XS, high signal was
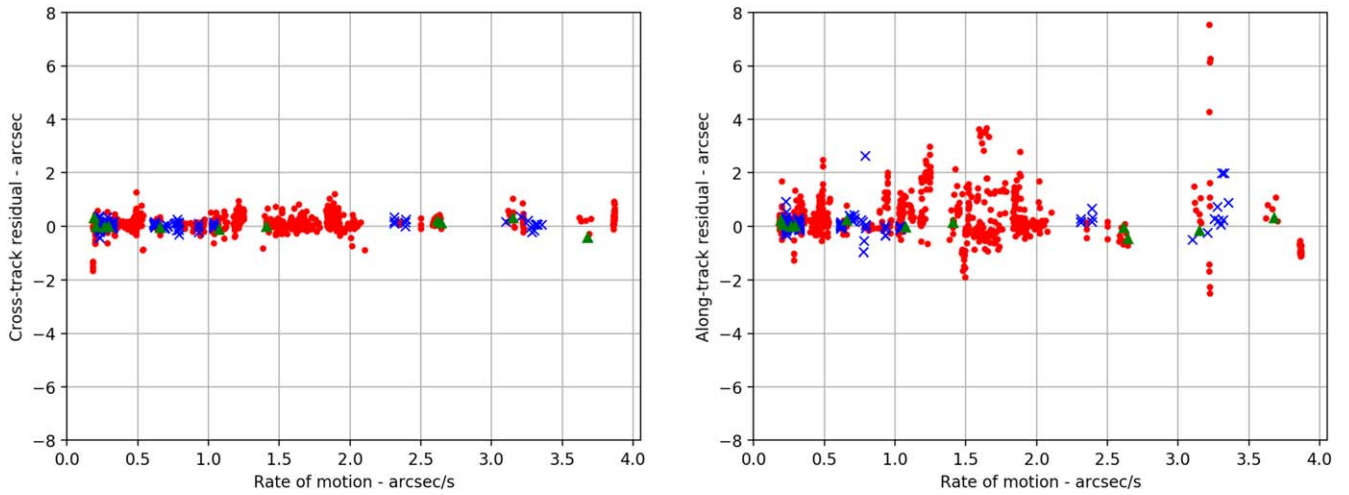
Figure 4. Magnitude of cross-track (left panel) and along-track (right panel) residuals of the observations collected as part of the campaign as a function of the plane-of-sky rate of motion. Crosses correspond to survey observations, circles to targeted observations, and triangles to the calibration observations included in the fit. The two panels use the same scale to highlight the larger along-track residuals.
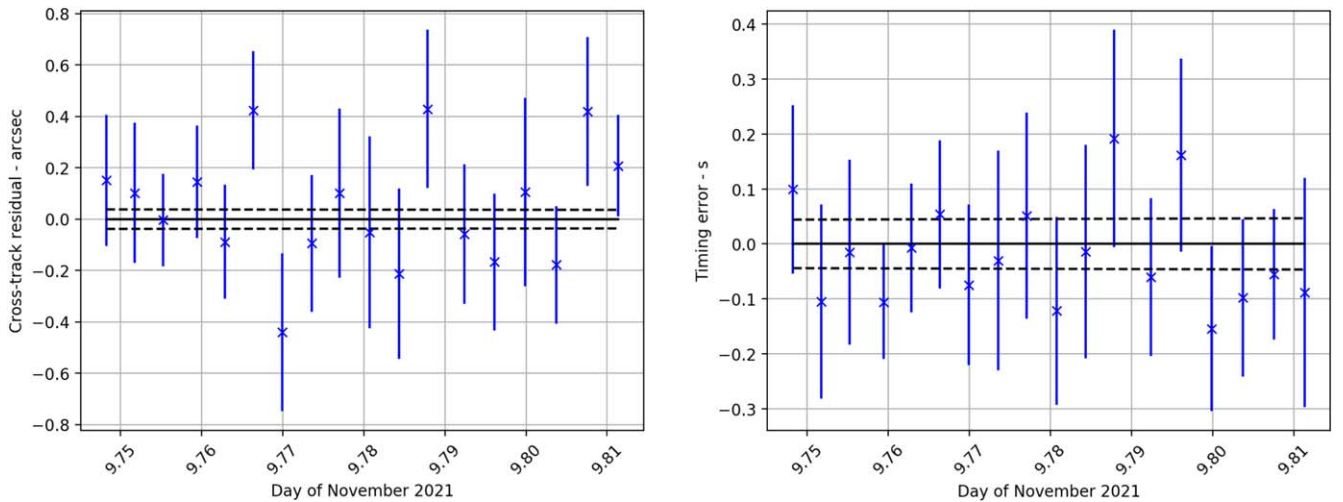

Figure 5. Cross-track (left panel) and timing (right panel) errors (crosses) and 1σ error bars for a selected tracklet of observations collected by N82 during the campaign when the plane-of-sky rate of motion of 2019 XS was $2'' \, s^{-1}$. The dashed line corresponds to the orbit solution uncertainty. The cross-track and timing errors do not show any significant bias, and the estimated uncertainties are consistent with the errors.

easy to obtain with short exposures, which avoid trailing. Therefore, follow-up observations could be executed using short exposure times, while surveys, which observed 2019 XS as part of their pipeline operations, used longer exposures times than necessary for this object.

6. Discussion

Given the results presented in Section 5, we now discuss some general guidelines to improve the accuracy of astrometric measurements and the uncertainty estimation process. Moreover, we suggest possible causes for the observed time errors to help diagnostic efforts to identify and correct the resulting biases.

6.1. Star Catalog

The accuracy of an astrometric observation is affected by that of the reference star catalog used in the astrometric reduction process. As a matter of fact, debiasing schemes have

been developed to correct asteroid astrometry from star catalog systematic errors (e.g., Eggl et al. 2020). The Gaia mission (Gaia Collaboration et al. 2016b) represents a major advance in the field, as it has provided star catalogs whose accuracy is orders of magnitude better than any other existing catalogs in all magnitude regimes that are meaningful for asteroid astrometry.

Therefore, to derive astrometric positions, observers are strongly encouraged to adopt one of the Gaia star catalogs. The first data release (Gaia Collaboration et al. 2016a) has the limitation of lacking stellar proper motions and so should no longer be used. While any release starting from DR2 (Gaia Collaboration et al. 2018) will be sufficiently accurate, later releases such as EDR3 (Gaia Collaboration et al. 2021) are preferable. There are other catalogs such as the ATLAS All-Sky Stellar Reference catalog (Tonry et al. 2018) that use Gaia for the astrometric coordinates of their sources, while including additional information (e.g., magnitudes) from other sources. These catalogs are also acceptable for astrometric use, once it is
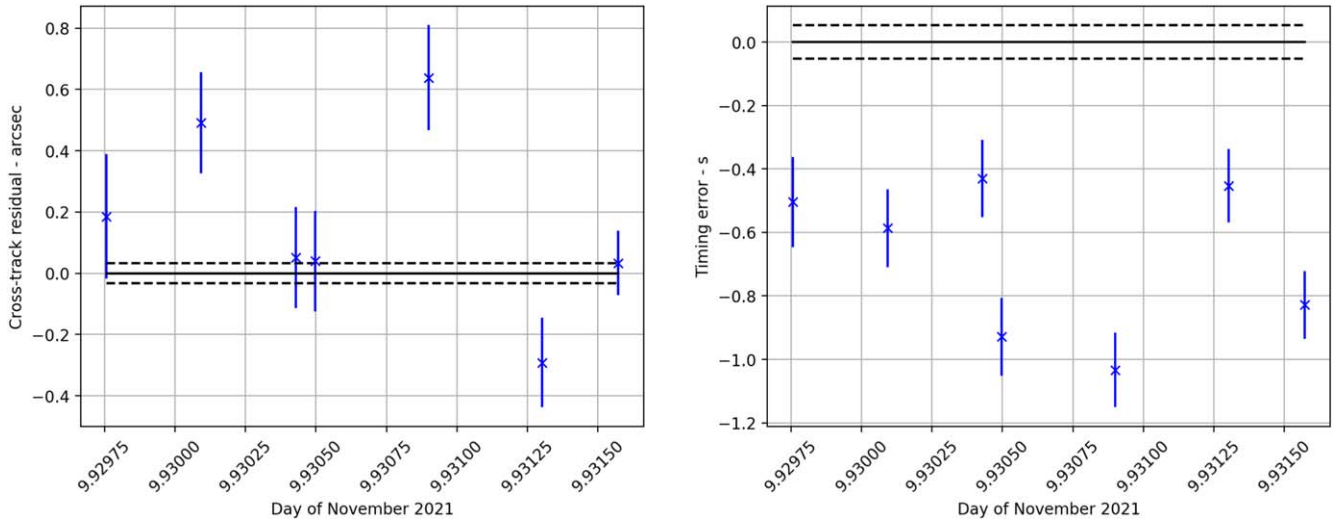
Figure 6. Cross-track (left panel) and timing (right panel) errors (crosses) and 1σ error bars for a second example of tracklet of observations collected by Y00 during the campaign when the plane-of-sky rate of motion of 2019 XS was $1{.}''5\,\mathrm{s}^{-1}$. The dashed line corresponds to the orbit solution uncertainty in the along-track direction scaled by the rate of motion. The cross-track errors do not show any evident bias, but the estimated uncertainties underestimate the actual errors. The timing residuals suggest that there is a systematic timing error of $-0.7\,\mathrm{s}$.
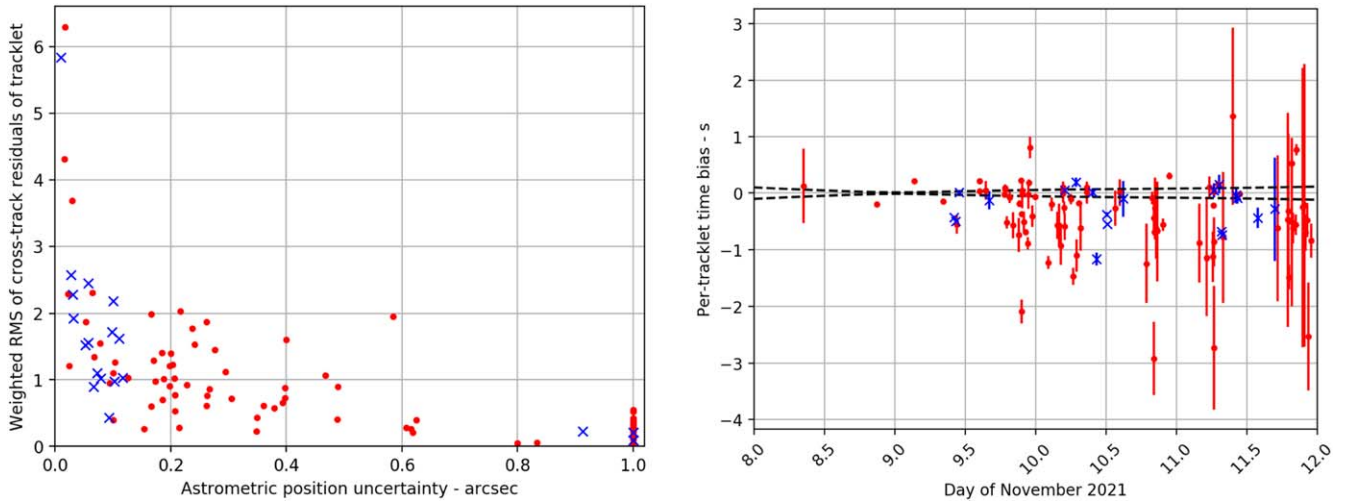
Figure 7. Left: weighted rms of the cross-track residuals of each tracklet as a function of the astrometric position uncertainties. Right: estimated mean timing error (b_T) for each tracklet of observations considered in our analysis. Crosses correspond to survey data, and circles correspond to follow-up data. The dashed line corresponds to the orbital uncertainty mapped into the along-track direction in the plane of sky and converted to time using the rate of motion.

fully verified that the stellar coordinates and proper motions are exactly the same as those of Gaia and that the catalog is complete to the same depth (especially for observers that reach faint limiting magnitudes).

Table 4 shows the different star catalogs used during this campaign and the corresponding number of observations. About 80% of the observations were reduced against the Gaia (DR2 or EDR3) and ATLAS catalogs. However, there is still a significant fraction of observations based on older, less accurate catalogs or for which no catalog was reported. A final comment is that no observation should be reported without specifying the star catalog used.

6.2. Stacking

The brightness of 2019 XS during its flyby was sufficient to allow even small-aperture amateur-level instruments to easily detect the object in very short exposures. However, fainter objects require longer exposure times, and if they are particularly fast, it quickly becomes impossible to detect the object in an individual exposure without allowing for either the object or the field stars to trail.

The simplest solution to this issue is to move the telescope at the expected rate of motion of the object, producing an image where the target is a point source, while the stars are visible as long trails. However, the astrometric solution for this image then needs to be determined using these trailed stars, which may not be a feature of commonly available software packages.

The most widely used alternative approach in these circumstances is stacking: single shorter-exposure images are combined together after acquisition, co-adding them with a relative offset that corresponds to the motion of the asteroid. It is important to mention that different stacks must be independent, and thus the same image cannot be used for two different stacks. This approach results in a final frame that looks similar to the previous solution,

with a point-like target and trailed field stars. However, those field stars can now be measured on the individual frames that composed the stack, where they look point-like, and therefore can be centroided with normal tools. This process works extremely well in most cases, because it also allows additional flexibility in the post-processing (e.g., individual contaminated frames can be excluded, or the images can be stacked nonlinearly if the object had nonlinear motion during the observing window). However, the stacking method comes with an additional complication: the target is measured on the stacked frame, but the stars (and therefore the astrometric transformations) are determined on just one of the exposures. In order for the measured position to match the associated time tag, the observer should ensure that the reported time corresponds to the time of the exposure that was used for the stack, or that the two have been properly shifted in a consistent way to ensure that there is a match between the reference frame and the time of the measurement. If this is not done properly, the reported astrometry will show evidence of a bias in the along-track direction.

Another consideration specific to short exposures is that over short timescales seeing causes random displacements of point sources, which in turn contribute to astrometric errors. Under these conditions, averaging by stacking can improve the accuracy of the measured position of the asteroid.

6.3. Number of Observations to Be Reported

While in a perfect Gaussian scenario increasing the number of observations helps to reduce the level of noise, the results of Section 5 demonstrate the presence of systematic errors. To prevent these systematic errors from biasing the orbital solutions, it makes sense to limit the observations to be reported to the MPC. Four observations per night from the same observer represent a reasonable compromise: there are enough observations to ensure the reliability of the detection and provide rate of motion information, but the number is sufficiently low to mitigate the effect of systematic errors. Reporting more than four observations per night rarely helps the orbit solution, and the resulting data may end up being deweighted (see, e.g., Vereš et al. 2017). A gap of about 24 hr between consecutive same-observer submissions significantly reduces the correlation between the observation data sets (Baer et al. 2011).

In some circumstances it might make sense to collect a larger number of observations. For instance, in the context of this campaign, a larger number of observations were warranted, as the goal was that of measuring systematic errors rather than improving the orbit solution. Another example is light-curve analysis, where a complete sampling of the rotation period provides information on the rotation state of the target. Especially in cases as bright as 2019 XS, short exposures enable a larger number of images. However, when the astrometry is reported to the MPC to be used for orbit estimation, the observer should down-sample the data set and only select a handful of positions (e.g., four). It is important to point out that the selection of the positions to be reported should not be based on orbital fits, e.g., by choosing the positions with the smallest residuals. Doing so would result in a data set that does not correctly capture the level of noise of the data and would bias the solution toward the orbital fit performed, which may or may not be correct. A uniform coverage in time, perhaps maximizing the time interval, would be a preferred approach. On the other hand, a sanity check on

the residuals could be useful to identify and resolve macroscopic problems with the astrometric reduction process and the compilation of the observation report.

6.4. Estimation of Astrometric Uncertainties

Given the fact that a significant number of reported position uncertainties underestimated the true extent of astrometric errors, we present a simple formulation to estimate astrometric uncertainties. This approach is conservative, represents a good starting point that anybody can use, and is based on information and components that are commonly provided by most astrometric software packages such as Astrometrica,[75] Tycho Tracker,[76] and AstroMagic.[77]

The astrometric uncertainty of a measurement is basically the combination of three components:

1. centroiding error, i.e., how well the center of the object is determined;
2. astrometric solution error, i.e., the error in the transformation that maps pixel coordinates into R.A. and decl.; and
3. any local bias of the astrometric solution.

In turn, the astrometric solution error is the combination of two terms:

2a. error in the stellar positions of the reference catalog; and
2b. discrepancies between the astrometric model and the features of the image, e.g., distortion of the field.

Using one of the Gaia catalogs as recommended in Section 6.1 allows one to entirely neglect component 2a and most of component 3. In fact, the catalog is much more accurate than the measured positions of our reference stars (milliarcsecond level), and thus the catalog itself is not introducing any significant bias. We now want to describe a procedure to conservatively estimate the contributions of the other components.

Centroiding errors (component 1) are very simple to estimate with a first-order approximation. Given the signal-to-noise ratio S of the measurement and the FWHM θ of the object's point-spread function, a conservative estimate of the centroiding error is $E_1 = \theta/(2S)$. When the source is trailed, centroiding can become more complex, and more sophisticated trail-fitting techniques (Vereš et al. 2012) are warranted to properly assess the correlated α and δ uncertainty covariance.

Astrometric solution errors are harder to assess because they depend on how well your astrometric solution matches the actual distortions of the focal plane (component 2b) and also on other possible noncharacterized biases (e.g., differential chromatic refraction; Stone 2002; Geykhman & Cahoy 2018) affecting the local solution (component 3). To properly determine the actual contribution of these components, one would first have to perform a statistical test of how well the adopted astrometric model (e.g., the order of the fit: linear, quadratic, cubic) matches plate distortions. Then, from a least-squares fit one can derive the polynomial coefficient and their error bars. Finally, when the order of the fit is chosen, the uncertainties of the fit need to be mapped to the uncertainty of the measured position on the plate. This process is not trivial

---

[75] http://astrometrica.at/
[76] https://www.tycho-tracker.com/
[77] http://astromagic.it/

Table 3
Fraction of Tracklets with Weighted rms of the Residuals Greater Than 1

Uncertainty	$<0\overset{''}{.}05$	$0\overset{''}{.}05–0\overset{''}{.}1$	$0\overset{''}{.}1–0\overset{''}{.}2$	$0\overset{''}{.}2–0\overset{''}{.}5$	$>0\overset{''}{.}5$
Fraction	100%	73%	62%	39%	3%

Note. A weighted rms > 1 indicates that the estimated uncertainties underestimate the actual extent of the astrometric position errors.

Table 4
Number of Campaign Observations for Each Star Catalog

Star Catalog	Number of Observations	Fraction	References
Unknown	62	6.5%	
USNO-A2.0	8	0.8%	Monet (1998)
USNO-B1.0	30	3.1%	Monet et al. (2003)
2MASS	36	3.8%	Skrutskie et al. (2006)
UCAC-3	19	2.0%	Zacharias et al. (2010)
UCAC-4	27	2.8%	Zacharias et al. (2013)
Gaia DR1	8	0.8%	Gaia Collaboration et al. (2016a)
Gaia DR2	731	76.4%	Gaia Collaboration et al. (2018)
Gaia EDR3	33	3.4%	Gaia Collaboration et al. (2021)
ATLAS-2	3	0.3%	Tonry et al. (2018)

and is not employed by the most commonly used astrometric software packages.

However, we can err on the side of caution and use an admittedly conservative estimate of the astrometric solution error, which takes component 2b into account and also mitigates possible unknown causes of biases (component 3). The solution is simply to take the rms of the astrometric fit, which is generally provided by the astrometric software, as the second component of the astrometric error E_2. The rms of the astrometric fit is a measure of how far the field stars are from where they should be. It is a combination of different contributions such as how well the star itself is detected and whether its position is locally biased. Since we generally have dozens of stars in the field, each one of them contributes to the astrometric solution, and if no biases are present, the overall solution has errors smaller than the rms (by $\sim \sqrt{N}$, where N is the number of stars used in the solution). However, the error is unlikely to be worse than the rms, since it quantifies the average of how badly sources are measured in the image. Therefore, we can conservatively assume the astrometric solution contribution to the uncertainty to be E_2.

The overall uncertainty of the measurement can therefore be written as $E = \sqrt{E_1^2 + E_2^2}$. In general, the rms of the solution may be different in α and δ, and the centroiding covariance might be nondiagonal. In this case the combination of the different error sources can be obtained by adding the corresponding covariance matrices. As an example for a typical error budget calculation, we can use the first observation reported by code L80 on 2021 November 8.868574 UTC. The object is clearly detected in the image, with a signal-to-noise ratio of $S = 8$. Due to the very low altitude of the field above the horizon, just $16°$, the FWHM of the detection is $\theta = 5''$. Therefore, the first component of the error budget is $E_1 = 5''/(2 \times 8) \sim 0\overset{''}{.}31$. The Gaia DR2−based astrometric solution of that plate, performed with fourth-degree polynomials on all Gaia stars down to magnitude 18, has an

astrometric rms of $E_2 = 0\overset{''}{.}22$. Adding the two error contributions in quadrature, we obtain $E = 0\overset{''}{.}38$, which we rounded to $0\overset{''}{.}4$.

This approach is purposely conservative. Each component of the error budget is estimated by erring on the safe side.

6.5. Station Position

The MPC provides the location of the observing sites.[78] Any error in station position Δ_{STN} would manifest as a systematic astrometric error $\propto \Delta_{STN}/\rho$, where ρ is the topocentric distance to the target. It is therefore recommended to double-check the coordinates of the observing station, e.g., by using a GPS sensor, and report corrections to the MPC if necessary. The coordinates are to be referred to the World Geodetic System 1984 ellipsoid[79] and not to the geoid.

6.6. Timing

The most common cause for a timing issue, which can appear in any direction, is simply an erroneous or nonrecent time synchronization. For example, many observers use queries to a Network Time Protocol (NTP) server to synchronize the system. The synchronization should be repeated at regular and frequent intervals, but in some circumstances the connection may not be successful for one or multiple attempts. Not all synchronization tools properly deal with missed connections, resulting in the system clock drifting away from the proper timing. Similar issues may happen if a GPS receiver is used to obtain an accurate time stamp. In all these cases, the solution is simply to make sure that these connections are successful, or at least that the observer is notified in case of a failed synchronization.

Once synchronization issues are taken care of, other hidden causes may be responsible for additional biases, and the sign of the bias may provide hints on the possible source. For example, the analysis presented above shows that the majority of the timing biases detected during the campaign are negative, meaning that the time tag reported with the astrometry is earlier than it should have been, on the basis of the object's position. The following is a nonexhaustive list of a few common sources of negative timing biases that have been encountered by the authors in actual telescopic systems:

1. The most common source of a negative time bias is a mechanical delay between the command to open the shutter and the actual motion of the physical device. In most systems, this hardware delay can easily account for a few tenths of second of delay, but there are systems that execute other steps between the command and the mechanical motion, introducing further delays that may add up to a few seconds. These delays are fortunately typically very stable and reproducible and can therefore be measured and compensated for. Shutter travel times across the field of view can be mapped by taking a picture of a constantly illuminated field (e.g., a dome flat) using different short exposure times. Each point of the focal plane will be exposed for different times, revealing the shutter pattern. One can also determine how the received flux varies for each exposure time and extrapolate the actual loss of light of each point and in turn the travel time. If the effect turns out to be significant, the modeled

---

travel times can also be compensated for, once the position of the source on the focal plane is known.

2. A second source of possible biases is due to the finite travel time of the shutter over the focal plane of the detector. In most small-size instruments the physical distance traveled by the shutter is small, and therefore the different pixels are typically exposed within a few tenths of a second of each other. However, for larger focal planes, including in professional telescopes, it is not unusual for the shutter to require seconds to transit from one side to the other, or to go from a fully closed to a fully open position. This is often due to the fact that professional cameras are designed with photometric consistency in mind, and therefore a significant design effort is placed to ensure that the total integration time is well controlled, at the cost of reduced speed and timing accuracy of the shutter event. Shutter travel times can also be modeled and compensated for, once the position of the source on the focal plane is known. However, in some cases information on the specific opening pattern is needed: for example, some shutters open and close on alternating sides of the focal plane, and therefore the same pixel may be the first to expose on some frames and the last to expose on some others. This information needs to be available in order to properly correct the time.

3. There are cameras that perform some purely electronic steps between the command to expose and the actual exposure start. For example, they may flush or pre-clear the detector, or automatically download a bias exposure. In some cases, these delays are not reflected in the time stamp, resulting in delays of many seconds. More generally, there can be software execution latency that causes timing errors.

4. Another delicate source of biases is purely numerical. Some cameras save time tags with the precision of 1 s, but this tag is sometimes a truncation, not a rounding, of the actual time of execution. This may account for systematic biases of a half second on average, with peaks of 1 s when the truncation happens in the worst possible scenario.

5. Finally, a common source of a negative timing bias is the erroneous choice to report the start of exposure time as the time tag of an astrometric observation. For single exposures, the reference time to be reported to the MPC is the mid-time of the exposure, computed as the average between the open and close shutter times, or equivalently by adding half of the overall exposure duration to the start time stamp. This error is typically easy to spot for long exposures, but it might not be easily noticeable for shorter ones.

Sources of positive time biases are rarer and typically harder to track down. A short list may include the following circumstances:

1. A not uncommon cause of positive biases, typically very noticeable, is the assumption that a time tag is expressed in UTC, while in reality it was defined on a different timescale. Common occurrences are writing either GPS or TAI time tags in keywords that are expected to contain UTC times. The differences between these scales are nevertheless very large (tens of seconds), and therefore they are typically easy to identify.

2. A rarer but possible issue is the use of a keyword typically expected to contain a start time to distribute a later time, e.g., the time of the middle or end of the exposure, or even the time when the entire exposure is downloaded. This is a particularly dangerous situation because any test performed using a single exposure time will lead to results that can be interpreted as a constant time bias. The recommendation is to use different exposure times when testing for timing accuracy, in order to highlight situations that depend on end of exposure events.

3. Similarly to negative time errors, an incorrect time approximation by the astrometric reduction software can cause a positive bias, e.g., if the time is rounded up to the nearest integer second.

6.7. Reporting Format

The IAU ADES format (Chesley et al. 2017) allows observers to report uncertainty information. ADES was successfully used to report 57% of the observations collected during the campaign, and we solicit its widespread adoption by the observing community. While schemes (e.g., Vereš et al. 2017) have been devised to properly weight and account for the uncertainty of the data, these schemes generally assume uniform quality for observations by the same observer. However, the astrometric uncertainty is a specific property of the individual observation. Therefore, knowing the uncertainty as estimated by the observer would greatly help in devising higher-fidelity weighting schemes and improve the accuracy of the estimated orbit solutions. For instance, Wainscoat et al. (2020) show that using astrometric uncertainties estimated by Pan-STARRS improved the predictions on the following night for new discoveries.

7. Conclusions

The reliability of the trajectory estimation for asteroids strongly depends on the accuracy of astrometric observations used in the fit and their statistical treatment. Therefore, the identification of sources of systematic errors and their removal can significantly improve the accuracy of the estimated orbits. As an example, errors in the reference star catalog map into errors in the measured astrometric position of the asteroid. Star catalog debiasing schemes can help correct for the resulting biases and lead to more accurate orbital solutions (Chesley et al. 2010; Farnocchia et al. 2015; Eggl et al. 2020). Recent star catalogs such as Gaia DR2 (Gaia Collaboration et al. 2018) and Gaia EDR3 (Gaia Collaboration et al. 2021) have star positions measured to the milliarcsecond level, and thus the corresponding errors become irrelevant for routine optical astrometry of asteroids.

A little characterized source of error for asteroid observations is related to the reported time of observation. Any time error maps into plane-of-sky errors as a function of the rate of motion. Fast movers during close approaches to Earth are particularly affected. The close approach of 2019 XS to Earth on 2021 November 9 represented a good opportunity to assess the accuracy of the reported observation times. In fact, the high rate of motion and brightness, together with its well-constrained orbit, enabled a statistical analysis of the astrometric data.

We collected 957 astrometric positions of 2019 XS from 2021 November 8.0 to 12.0 UTC. For the 921 observations that were collected with ground-based telescopes we analyzed the corresponding residuals in the cross-track and along-track

directions. The along-track direction is aligned with the plane-of-sky motion, and therefore along-track residuals can be used to characterize timing errors. We found that timing errors are typically smaller than 1 s. However, there is a prevalence of negative values, i.e., the reported times are generally biased toward early values. The identification and resolution of the root cause of the observed bias are beyond the scope of this paper and are left to the individual observers. To help with diagnostic efforts, we provided observers with individual, detailed reports and suggested possible explanations related to the telescope mechanics and software implementation. Observers are encouraged to regularly calibrate their timing, e.g., by observing GPS satellites or by participating in similar observation campaigns in the future.

The cross-track residuals are completely independent of timing errors and therefore are a pure manifestation of positional errors that can be compared to the adopted uncertainties. This comparison is particularly useful for observations where the uncertainty was quantified and reported by the observers. In particular, 543 observations were reported to the MPC using the ADES format (Chesley et al. 2017), which includes specific fields for astrometric uncertainties. As the reported uncertainties decrease, especially when $<0\rlap{.}{''}2$, they generally fail to capture the full extent of the position error. The implication is that some sources of error (e.g., errors in the plate solution) may be neglected in the uncertainty budget. We presented a recipe to quantify astrometric uncertainties that is simple and conservative and can therefore help observers in reporting more reliable uncertainties.

ORCID iDs

Davide Farnocchia https://orcid.org/0000-0003-0774-884X
Vishnu Reddy https://orcid.org/0000-0002-7743-3491
James M. Bauer https://orcid.org/0000-0001-9542-0953
Elizabeth M. Warner https://orcid.org/0000-0003-1147-4474
Marco Micheli https://orcid.org/0000-0001-7895-8209
Matthew J. Payne https://orcid.org/0000-0001-5133-6303
Tony Farnham https://orcid.org/0000-0002-4767-9861
Mirel Birlan https://orcid.org/0000-0003-3495-8535
Bryce T. Bolin https://orcid.org/0000-0002-4950-6323

Melissa J. Brucker ⑩ https://orcid.org/0000-0002-2079-179X
Kenneth C. Chambers ⑩ https://orcid.org/0000-0001-6965-7789
Anlaug A. Djupvik ⑩ https://orcid.org/0000-0001-6316-9880
Leonid Elenin ⑩ https://orcid.org/0000-0001-9336-9648
Randy Flynn ⑩ https://orcid.org/0000-0002-4562-2204
Mikael Granvik ⑩ https://orcid.org/0000-0002-5624-1888
Myung-Jin Kim ⑩ https://orcid.org/0000-0002-4787-6769
David Lane ⑩ https://orcid.org/0000-0002-6097-8719
Hee-Jae Lee ⑩ https://orcid.org/0000-0002-6839-075X
Bin Li ⑩ https://orcid.org/0000-0001-9327-0920
Tim Lister ⑩ https://orcid.org/0000-0002-3818-7769
Eugene A. Magnier ⑩ https://orcid.org/0000-0002-7965-2815
Dan A. Nedelcu ⑩ https://orcid.org/0000-0001-5684-9896
Marcel Popescu ⑩ https://orcid.org/0000-0001-8585-204X
Dong-Goo Roh ⑩ https://orcid.org/0000-0001-6104-4304
Filipp D. Romanov ⑩ https://orcid.org/0000-0002-5268-7735
Toni Santana-Ros ⑩ https://orcid.org/0000-0002-0143-9440
Sergei Schmalz ⑩ https://orcid.org/0000-0001-5783-3888
Robert Seaman ⑩ https://orcid.org/0000-0001-9385-8978
Nick Sioulas ⑩ https://orcid.org/0000-0002-2012-1227
Adrian B. Sonka ⑩ https://orcid.org/0000-0001-5465-5449
David J. Tholen ⑩ https://orcid.org/0000-0003-0773-1888
Madalina M. Trelia ⑩ https://orcid.org/0000-0003-2362-4230
Richard Wainscoat ⑩ https://orcid.org/0000-0002-1341-0952
Guy Wells ⑩ https://orcid.org/0000-0002-6667-6535
Robert Weryk ⑩ https://orcid.org/0000-0002-0439-9341
Quanzhi Ye ⑩ https://orcid.org/0000-0002-4838-7676
Hong-Suh Yim ⑩ https://orcid.org/0000-0001-5484-4741
Chengxing Zhai ⑩ https://orcid.org/0000-0002-0291-4522
Chen Zhang ⑩ https://orcid.org/0000-0002-9583-263X
Tinglei Zhu ⑩ https://orcid.org/0000-0002-0850-8824

References

Baer, J., Chesley, S. R., & Milani, A. 2011, Icar, 212, 438
Carpino, M., Milani, A., & Chesley, S. R. 2003, Icar, 166, 248
Chesley, S. R., Baer, J., & Monet, D. G. 2010, Icar, 210, 158
Chesley, S. R., Hockney, G. M., & Holman, M. J. 2017, AAS/DPS Meeting, 49, 112.14
Eggl, S., Farnocchia, D., Chamberlin, A. B., & Chesley, S. R. 2020, Icar, 339, 113596
Farnocchia, D., Chesley, S. R., Chamberlin, A. B., & Tholen, D. J. 2015, Icar, 245, 94
Farnocchia, D., Chesley, S. R., Vokrouhlický, D., et al. 2013, Icar, 224, 1
Gaia Collaboration, Brown, A. G. A., Vallenari, A., et al. 2016a, A&A, 595, A2
Gaia Collaboration, Brown, A. G. A., Vallenari, A., et al. 2018, A&A, 616, A1
Gaia Collaboration, Brown, A. G. A., Vallenari, A., et al. 2021, A&A, 649, A1
Gaia Collaboration, Prusti, T., de Bruijne, J. H. J., et al. 2016b, A&A, 595, A1
Geykhman, R., & Cahoy, K. 2018, Proc. SPIE, 10702, 107024U
Monet, D. G. 1998, AAS Meeting, 193, 120.03
Monet, D. G., Levine, S. E., Canzian, B., et al. 2003, AJ, 125, 984
Reddy, V., Kelley, M. S., Dotson, J., et al. 2022a, Icar, 374, 114790
Reddy, V., Kelley, M. S., Dotson, J., et al. 2022b, PSJ, 3, 123
Reddy, V., Kelley, M. S., Farnocchia, D., et al. 2019, Icar, 326, 133
Seidelmann, P. K. 1977, CeMec, 16, 165
Skrutskie, M. F., Cutri, R. M., Stiening, R., et al. 2006, AJ, 131, 1163
Stone, R. C. 2002, PASP, 114, 1070
Tonry, J. L., Denneau, L., Flewelling, H., et al. 2018, ApJ, 867, 105
Vereš, P., Farnocchia, D., Chesley, S. R., & Chamberlin, A. B. 2017, Icar, 296, 139
Vereš, P., Jedicke, R., Denneau, L., et al. 2012, PASP, 124, 1197
Vereš, P., Payne, M. J., Holman, M. J., et al. 2018, AJ, 156, 5
Vokrouhlický, D., Bottke, W. F., Chesley, S. R., Scheeres, D. J., & Statler, T. S. 2015, in Asteroids IV, ed. P. Michel et al. (Tucson, AZ: Univ. Arizona Press), 509
Wainscoat, R. J., Weryk, R., & Farnocchia, D. 2020, in 2020 IEEE Aerospace Conf. (Piscataway, NJ: IEEE), 1
Zacharias, N., Finch, C., Girard, T., et al. 2010, AJ, 139, 2184
Zacharias, N., Finch, C. T., Girard, T. M., et al. 2013, AJ, 145, 44